

**Hot and dense homogeneous nucleonic matter constrained by observations, experiment, and theory**Xingfu Du,<sup>1</sup> Andrew W. Steiner,<sup>1,2</sup> and Jeremy W. Holt<sup>3</sup><sup>1</sup>*Department of Physics and Astronomy, University of Tennessee, Knoxville, Tennessee 37996, USA*<sup>2</sup>*Physics Division, Oak Ridge National Laboratory, Oak Ridge, Tennessee 37831, USA*<sup>3</sup>*Cyclotron Institute and Department of Physics and Astronomy, Texas A&M University, College Station, Texas 77843, USA*

(Received 12 March 2018; published 11 February 2019)

We construct a new class of phenomenological equations of state for homogeneous matter for use in simulations of hot and dense matter in local thermodynamic equilibrium. We construct a functional form which respects experimental, observational, and theoretical constraints on the nature of matter in various density and temperature regimes. Our equation of state (EOS) matches (i) the virial coefficients expected from nucleon-nucleon scattering phase shifts, (ii) experimental measurements of nuclear masses and charge radii, (iii) observations of neutron star radii, (iv) theory results on the equation of state of neutron matter near the saturation density, and (v) theory results on the evolution of the EOS at finite temperatures near the saturation density. Our analytical model allows one to compute the variation in the thermodynamic quantities based on the uncertainties in the nature of the nucleon-nucleon interaction. Finally, we perform a correction to ensure the equation of state is causal at all densities, temperatures, and electron fractions.

DOI: [10.1103/PhysRevC.99.025803](https://doi.org/10.1103/PhysRevC.99.025803)**I. INTRODUCTION**

The equation of state (EOS) of dense nucleonic matter is a central microphysical input required for numerical simulations of core-collapse supernovas [1] and neutron star mergers [2]. These simulations probe baryon densities ( $n_B$ ) up to a few nucleons per fm<sup>3</sup>, temperatures ( $T$ ) up to 100 MeV, and a wide range of electron fractions ( $Y_e$ ). This three-dimensional space is often described through an EOS table which relates the free energy or pressure of the system to the thermodynamic variables describing the ambient environment. These tables, in turn, are built from modeling the interactions between nucleons, nuclei, and potentially exotic particles that may appear at high densities.

Over this large three-dimensional ( $n_B, Y_e, T$ ) space, there are several different physical regimes each constrained by different observables and theoretical approaches. The first regime, zero temperature nuclear matter at nuclear saturation density, is closely connected to nuclear masses, charge radii, giant resonances, and other laboratory observables. Global fits to experimental data have been performed with Skyrme (e.g., Ref. [3]) and covariant mean-field models (e.g., Ref. [4]). The second regime, cold neutron matter below nuclear saturation density, is difficult to probe experimentally but is well constrained by theoretical calculations based on semi-phenomenological nuclear forces or microscopic chiral effective field theory-based interactions [5–7]. The third regime, strongly interacting high-temperature matter, is best described by interactions and many-body approaches similar to those applied to cold neutron matter near saturation density [8–11]. The fourth regime, low-density and high-temperature matter that is nearly nondegenerate, is best described by the virial expansion. The equation of state in this regime is determined from nucleon-nucleon scattering phase shifts [12,13]. Finally,

neutron-rich matter at densities above twice the saturation density is most strongly constrained by observations of neutron star masses and radii, particularly the observation of neutron stars with  $M \simeq 2M_\odot$  [14,15].

There are several currently available tabulated equations of state. The first set of EOSs, developed by Lattimer and Swesty (LS) [16], was constructed in the single-nucleus approximation and based on three different nonrelativistic Skyrme interactions. Two of the three Skyrme interactions have nuclear incompressibilities ( $K$ ) far outside of modern constraints [17,18]. The third, with  $K = 220$  MeV, has a combination of symmetry energy ( $S$ ) and slope of the symmetry energy ( $L$ ) that is only slightly outside of current constraints [19–22]. The LS EOS with  $K = 220$  MeV also produces a  $2M_\odot$  neutron star and is still important for simulations of core-collapse supernovas and neutron star mergers. The second set of EOSs came from H. Shen *et al.* [23] (also using the single-nucleus approximation) and was based on the NL3 relativistic mean-field Lagrangian. The values of  $K$  and  $L$  for NL3 are much larger than current neutron star observations (see the analysis in, e.g., Ref. [24]) and nuclear theory [25] suggest.

While the single-nucleus approximation is sufficient to describe the bulk thermodynamics, it does not in general accurately describe the composition [26–31] and the associated weak reaction rates. More modern EOS tables often include a more complete nuclear distribution as a result. The third set from G. Shen *et al.* [32] includes an EOS table based on a more modern relativistic mean-field model, “FSUGold” [33], and goes beyond the single-nucleus approximation to include a full distribution of nuclei in nuclear statistical equilibrium (NSE). This model has values of  $K$ ,  $L$ , and  $S$  that are within recent constraints from experiment and (in later versions) produces a neutron star maximum mass larger than  $2M_\odot$ . These EOSs based on

FSUGold include more modern nuclear physics input, including a proper treatment of nearly nondegenerate matter that matches the virial expansion. The fourth set of EOS tables was based on the work of Hempel and others [34] that built upon several nucleon-nucleon interactions which produce reasonable values of  $K$ ,  $S$ , and  $L$  and generate  $2M_\odot$  neutron stars, including FSUGold, DD2 [35], IUFSU [36], SFHo [37] and SFHx [37]. The latter two interactions were designed to simultaneously match laboratory nuclei and give neutron star radii that match astronomical observations of neutron stars [24]. More recently, several EOSs have been added to the CompOSE (CompStar Online Supernovae Equations of State) database [38], including an EOS with hyperons [39].

In this work, we construct a phenomenological free energy density that is consistent with observational and theoretical constraints in the five aforementioned physical regimes. This is in contrast to works which attempt to describe matter over the entire density and temperature range with a single detailed model of the nucleon-nucleon interaction. Many previous works proceed this way using a Skyrme-based or relativistic mean-field model to describe matter at all densities and temperatures. The principal problem is that these models are guaranteed to work well only for isospin-symmetric nuclear matter at zero temperature. Extrapolating these models to other density and temperature regimes may lead to inaccurate EOS results or may introduce unphysical correlations between the nature of matter across different regimes. For example, given a Skyrme model it is common to observe that the nuclear incompressibility is correlated with the maximum mass of neutron stars. Such a correlation has little physical meaning, however, since the neutron star maximum mass is determined by interactions in high-density matter that likely have little similarity to nucleons in the laboratory (see a similar argument in Ref. [40]). We avoid extrapolations where possible, but some extrapolation will still be required where experimental and theoretical guidance is lacking.

Our second advance is in the treatment of uncertainties. The most relevant parameters which describe the uncertainties in different density and temperature regimes are not clearly related. The virial expansion provides a clear path forward for describing uncertainties at low density and high temperature, but higher-order virial terms are not necessarily useful for quantifying uncertainties at higher densities. In this work, through the construction of a phenomenological model one can vary uncertainties in different regimes independently, without spoiling agreement elsewhere.

## II. METHOD

The EOS table is constructed by combining an EOS for homogenous nucleonic matter consisting only of neutrons and protons. The EOS is written in the form of the Helmholtz free energy (including only the contribution from nucleons)  $f_{\text{np}}(n_B, Y_e, T)$ . In the discussion below, we remove the nucleon rest mass contributions from the free energy densities and chemical potentials and use a tilde when these rest mass contributions are included, i.e.,

$$\tilde{f}_{\text{np}}(n_B, Y_e, T) \equiv f_{\text{np}}(n_B, Y_e, T) + n_B[(1 - Y_e)m_n + Y_e m_p], \quad (1)$$

where  $m_n$  and  $m_p$  are the neutron and proton masses. When electrons are included, their rest mass contribution to the free energy is also included. We ignore muons because they are rarely included in simulations [41]. We also ignore exotic particles at higher densities. Thus the proton fraction,  $x_p$ , is always equal to the electron fraction,  $Y_e$ .

### A. Virial expansion and homogeneous nucleonic matter

The virial expansion is a model-independent way of computing the pressure of matter at low densities and high temperatures [12,13,42]. It is an expansion in powers of the fugacity,  $z_i$ , of particle  $i$  defined by

$$z_i = \exp(\mu_{i,\text{vir}}/T), \quad (2)$$

where  $\mu_{i,\text{vir}}$  denotes the nucleon chemical potential. In matter consisting only of neutrons and protons, the first-order terms in the pressure, proportional to  $z_n$  and  $z_p$ , consist of the classical noninteracting contribution to the pressure. The coefficients of the second-order terms (second-order virial coefficients) in the virial expansion can be obtained directly from nucleon-nucleon scattering phase shifts. Third-order virial coefficients are not well known. Nuclear statistical equilibrium implies that the fugacity of nuclei can be written in terms of the neutron and proton fugacities

$$z_{(Z,N)} \propto z_n^N z_p^Z. \quad (3)$$

Thus when the neutron and proton fugacities are nearly equal the contribution of deuterons comes at second order in the virial expansion and the contribution from  $\alpha$  particles comes at fourth order. Two-body scattering between nucleons and  $\alpha$  particles contributes at fifth order in the virial expansion. In this work, because the third-order virial coefficients are not well known, third- and higher-order terms are ignored.

Second-order terms in the virial expansion affect the description of homogeneous nucleonic matter. To ensure that the free energy matches the virial result at low densities and high temperatures, the free energy density is written as

$$f_{\text{np}}(n_B, x_p, T) = f_{\text{virial}}(n_B, x_p, T)g + f_{\text{deg}}(n_B, x_p, T)(1 - g), \quad (4)$$

where  $f_{\text{virial}}$  is the virial free energy density, and  $f_{\text{deg}}$  is the free energy density when either the neutrons or protons are sufficiently degenerate so that the virial expansion is a poor approximation. The function  $g$  is defined by

$$g \equiv 1/(1 + 3z_n^2 + 3z_p^2). \quad (5)$$

This definition ensures that  $(1 - g)f_{\text{deg}}$  appears as a third- or higher-order correction to the free energy density in the virial expansion as long as  $f_{\text{deg}}$  is at least linear in the fugacity at low densities (we verify this below). The value of  $g$  is 1 only when  $z_n$  and  $z_p$  are both sufficiently small. The numerical coefficient 3 was chosen to ensure a positive entropy in the entire region in  $(n_B, Y_e, T)$  space for which the pressure of our EOS is positive. The relationship between the fugacities and the densities is

$$\begin{aligned} n_n &= 2\lambda^{-3}[z_n + 2z_n^2 b_n(T) + 2z_n z_p b_{pn}(T)], \\ n_p &= 2\lambda^{-3}[z_p + 2z_p^2 b_n(T) + 2z_n z_p b_{pn}(T)]. \end{aligned} \quad (6)$$

These equations are solved for the fugacities in order to compute the free energy density from the virial expansion. The quantity  $\lambda \equiv [4\pi/(m_n T + m_p T)]^{1/2}$  is the average nucleon thermal wavelength, the quantity  $b_n(T)$  is the second neutron virial coefficient, and the quantity  $b_{pn}(T)$  is the virial coefficient describing the interaction between neutrons and protons.

The virial coefficients  $b_n(T)$  and  $b_{pn}(T)$  are determined by scattering phase shifts. Analytical fits can be employed, similar to those in Ref. [43], but previous fits for  $b_n$  employ functional forms which diverge for  $T \rightarrow 0$ . We perform an alternate fit, constraining the zero-temperature behavior to match that expected from a finite-range expansion, which will be correct when the density is sufficiently small. The values of the virial coefficients at high temperature are not well known, so we arbitrarily constrain the fits so that the virial coefficients give the value expected for noninteracting fermions at  $T = 150$  MeV. While very hot and nearly nondegenerate matter is present in simulations, it is unlikely to strongly affect the dynamics.

For the neutron matter virial coefficient, we use the data given in Refs. [12,13] and add three points at  $T = 0.1, 0.5$ , and  $150$  MeV, with virial coefficients of  $0.207, 0.272$ , and  $2^{-5/2}$ , respectively. The first two are determined from an effective range expansion to the phase shift with scattering length  $-18.9$  fm and effective range  $2.75$  fm as determined from Ref. [44]. The last value at  $T = 150$  MeV is the noninteracting result. We fit these data to a ten-parameter functional form

$$b_n(T) = b_0 + b_1 T + b_2 T^2 + b_3 T^3 + b_4 e^{-b_5(T-b_6)^2} + b_7 e^{-b_8(T-b_9)} \quad (7)$$

We find that the parameter set  $b_0 = 0.28745$ ,  $b_1 = 2.2006 \times 10^{-3} \text{ MeV}^{-1}$ ,  $b_2 = -2.6210 \times 10^{-5} \text{ MeV}^{-2}$ ,  $b_3 = 6.0617 \times 10^{-8} \text{ MeV}^{-3}$ ,  $b_4 = 1.0595 \times 10^{-2}$ ,  $b_5 = 5.6734 \times 10^{-2} \text{ MeV}^{-2}$ ,  $b_6 = 3.4925 \text{ MeV}$ ,  $b_7 = -2.7106 \times 10^{-3}$ ,  $b_8 = 3.1405 \text{ MeV}^{-1}$ , and  $b_9 = 1.2010 \text{ MeV}$  matches the data. The data and the fit are shown in the top panel of Fig. 1.

The contribution from the deuteron binding energy is typically included in  $b_{pn}(T)$ , but in this work the deuteron binding energy is removed. We do not yet include other bound states of nucleons (such as  $\alpha$  particles) so it would be inconsistent to include the deuteron. Nuclei will be added in a nuclear statistical equilibrium part of the free energy in a later work. For the low-temperature result ( $T < 1$  MeV), both  $^1S_0$  and  $^3S_1$  phase shifts contribute at low energy, while, due to the factor  $e^{-E/2T}$  from Eq. (22) in Ref. [13], it is reasonable to ignore the higher-order phase shift contributions. We use the scattering length  $-23.74$  fm and effective range  $2.77$  fm [44] for the  $^1S_0$  channel and the scattering length  $5.418$  fm and effective range  $1.833$  fm for the  $^3S_1$  channel from Ref. [45]. An alternate fit for  $b_{pn}$  is

$$b_{pn}(T) = c_0 e^{-c_1(T+c_2)^2} + c_3 e^{-c_4(T+c_5)}, \quad (8)$$

where  $c_0 = 1.5273$ ,  $c_1 = 1.7488 \times 10^{-4} \text{ MeV}^{-2}$ ,  $c_2 = 1.7550 \times 10^1 \text{ MeV}$ ,  $c_3 = 0.45104$ ,  $c_4 = 0.27513 \text{ MeV}^{-1}$ , and  $c_5 = -1.1250 \text{ MeV}$ . The data and the fit are shown in the bottom panel of Fig. 1.

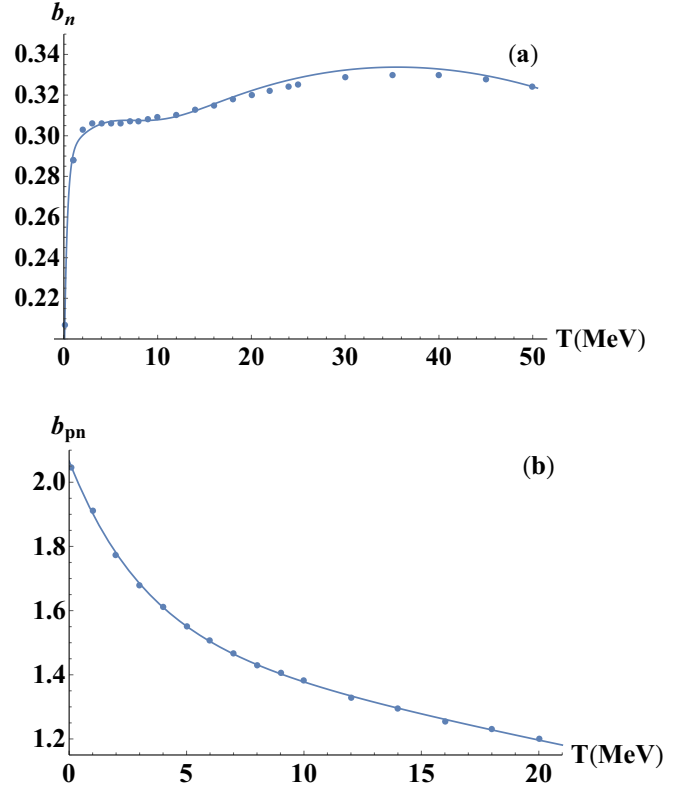


FIG. 1. Fit of virial coefficients to data. The points at  $T = 0.1$  MeV are computed through effective range expansion.

## B. First derivatives of the free energy

From Eq. (4), we can obtain the chemical potentials and entropy directly:

$$\mu_i = \mu_{i,\text{vir}} g + f_{\text{virial}} \frac{\partial g}{\partial n_i} + \frac{\partial f_{\text{deg}}}{\partial n_i} (1 - g) - f_{\text{deg}} \frac{\partial g}{\partial n_i} \quad (9)$$

for  $i = n, p$ , where

$$\mu_{i,\text{vir}} \equiv \frac{\partial f_{\text{virial}}}{\partial n_i} \quad (10)$$

and for the entropy

$$s = -\frac{\partial f_{\text{virial}}}{\partial T} g - f_{\text{virial}} \frac{\partial g}{\partial T} - \frac{\partial f_{\text{deg}}}{\partial T} (1 - g) + f_{\text{deg}} \frac{\partial g}{\partial T}. \quad (11)$$

To compute the derivatives of  $g$  with respect to the densities, one can differentiate Eqs. (6) with respect to  $n_n$  and  $n_p$  and then solve the resulting four equations for the quantities  $\partial \mu_{i,\text{vir}} / \partial n_j$  (for  $i, j = n, p$ ).

## C. Matter near nuclear saturation density

Experimentally measured nuclear masses are well described by Skyrme energy density functionals and thus it is expected that the energy density of nuclear matter at zero temperature is also well described by the Skyrme model. In Ref. [3], the parameters of the Skyrme model were fit to several nuclear masses, charge radii, and pairing energies using Bayesian inference. We use a set of 1000 Skyrme

parametrizations selected from the posterior distribution computed in Ref. [3] to describe isospin symmetric matter.

Because there is relatively little information from theory or experiment in some regimes, the Skyrme model will also be extrapolated to higher densities and temperatures from below. This means that, however, we cannot use all of the parametrizations because some of them have a nucleon effective mass which becomes negative for densities below  $n_B < 2 \text{ fm}^{-3}$ . We remove such Skyrme models from consideration.

Nuclear mass measurements are restricted to relatively isospin-symmetric nuclei; thus neutron matter is not necessarily accurately described by Skyrme models (see, e.g., the discussion regarding large fluctuations in the isovector channel in Ref. [46]). Zero-temperature neutron matter up to nuclear saturation density is tractable in quantum Monte Carlo [47] and many-body perturbation theory [7,48]. It has thus become common to fit to neutron matter calculations as well as nuclear mass data [49,50]. However, this practice presumes that the Skyrme functional is well suited to describing pure neutron matter, an assumption that is not necessarily valid. Thus, for pure neutron matter we use the four-parameter expression based on quantum Monte Carlo (QMC) results from Ref. [47],

$$\varepsilon_{\text{QMC}}(n_B) = f_{\text{QMC}}(n_B) = n_B \left[ a \left( \frac{n_B}{n_0} \right)^\alpha + b \left( \frac{n_B}{n_0} \right)^\beta \right]. \quad (12)$$

The range for the parameters  $0.47 < a < 0.53$  and  $12 < \alpha < 13$  MeV is chosen as in Ref. [51] to enclose the limits in Ref. [47].

The symmetry energy implied by many of the Skyrme fits, when combined with the quantum Monte Carlo results for neutron matter, naturally implies bound neutron matter at sub-saturation densities. Similarly, much of the range for  $S$  and  $L$  implied by the Skyrme parametrizations is outside the allowed range from Ref. [22]. Thus we ignore the values for  $S$  and  $L$  from the Skyrme models and limit  $L$  between 44 and 65 MeV, and  $S$  between 29.5 and 36.1 MeV as in Ref. [51]. These bounds are consistent with recent microscopic constraints [21] on the density dependence of the symmetry energy from chiral effective field theory. The prescription  $(9.17 S - 266 \text{ MeV}) < L < (14.3 S - 379 \text{ MeV})$  is used to ensure that  $S$  and  $L$  are correlated. The coefficients  $b$  and  $\beta$  are determined by

$$b = S - a + (E/A)_{\text{sky}}, \quad (13)$$

$$\beta = \frac{1}{b} \left( \frac{L}{3} - \alpha a \right), \quad (14)$$

where  $(E/A)_{\text{sky}}$  is the binding energy per particle of nuclear matter from the Skyrme interaction. Finally, we combine the nuclear matter and neutron matter results by assuming the symmetry energy is quadratic in  $x_p$ . This choice ensures that nuclear matter is representative of experimental results on nuclear masses while neutron matter agrees with modern theory results.

We note that the free energy density of matter from the QMC results above is always at least linear in the density, and by Eq. (6) at least linear in the fugacity at low densities. This also holds for the Skyrme model, since the kinetic part of the energy density is proportional to  $k_F^5$  and the potential energy

part is proportional to at least one power of the density. Thus our function  $g$  in Eq. (5) above is defined so that  $f_{\text{deg}}$  will leave the second-order virial coefficients unchanged from the values determined by experiment in the low-density limit.

#### D. Matter at high densities

Above nuclear saturation density, there are two principal sources for constraints on the EOS of matter: heavy ion collisions and neutron star observations. Constraints on the EOS from heavy ion collisions near the saturation density do not yet contradict results from Skyrme fits. However, constraints from heavy ion collisions on the EOS at higher densities do not yet provide a clear picture. Until the results from heavy ion collisions are more definitive, the Skyrme model from above is extrapolated to higher densities to describe isospin-symmetric nuclear matter.

Neutron star mass and radius observations constrain the equation of state of neutron-rich matter at high densities, in particular, the pressure as a function of the energy density [24]. Unfortunately, neutron star observations do not yet currently constrain the proton fraction of neutron star matter. We find that the form

$$\begin{aligned} \varepsilon_{\text{NS}}(n_B) &= f_{\text{NS}}(n_B) \\ &= p_0 n_B \sqrt{n_B} + p_1 n_B^2 + p_2 n_B^2 \sqrt{n_B} + p_3 n_B^3 + p_4 n_B^4 \end{aligned} \quad (15)$$

provides a good fit to the results from Ref. [24]. We randomly select EOSs from a Markov chain constructed in Ref. [51] and fit them to Eq. (15). Reference [51] constructed several Markov chains, and we use the chain which was constructed using the low-density neutron matter EOS from Ref. [47], model A (which models high-density matter using polytropes), and includes all of the mass and radius data from photospheric radius expansion x-ray bursts and quiescent low-mass x-ray binaries.

Astrophysical simulations can probe densities larger than those constrained by the neutron star data in Ref. [51]. Between a transition density,  $n_{Bf}$ , and the largest baryon density we consider,  $n_B = 2 \text{ fm}^{-3}$ , we implement a simple EOS adapted from Constantinou and Prakash [52] (hereafter denoted C&P). The procedure for matching these EOSs begins by setting  $n_{Bf}$  equal to the highest density specified by the Monte Carlo data in Ref. [51]. We decrease this transition density as necessary to ensure that the EOS from Eq. (15) is causal for densities lower than this transition density. We add an additional parameter,  $\phi$ , which is equal to the speed of sound at the largest density we consider,  $n_B = 2 \text{ fm}^{-3}$ .

The EOS between  $n_B = n_{Bf}$  and  $n_B = 2 \text{ fm}^{-3}$  is chosen depending on the relative magnitude of the speed of sound at these two end points. If the speed of sound is increasing with increasing baryon density, then we choose

$$c_s^2 = 1 - a_1 + \frac{a_1 a_2 n_B^{a_1}}{1 + a_2 n_B^{a_1}} \quad (16)$$

and determine  $a_1$  and  $a_2$  by matching the boundaries  $\equiv c_s^2(n_{Bf})$  and  $\phi = c_s^2(n_B = 2 \text{ fm}^{-3})$  thus ensuring  $\beta \rightarrow 1$  as



$n_B \rightarrow \infty$ . The energy density above  $n_B = n_{Bf}$  is

$$\varepsilon_{NS} = -m_n n_B + c_1 \left( \frac{1}{2} a_2 n_B^2 + \frac{n_B^{2-a_1}}{2-a_1} \right) + c_2, \quad (17)$$

where

$$c_1 = \frac{\varepsilon_f + m_n n_{Bf} + P_f}{n_{Bf}^2 (a_2 + n_{Bf}^{-a_1})},$$

$$c_2 = \frac{1}{2} \left[ (\varepsilon_f + m_n n_{Bf} - P_f) + a_1 \frac{\varepsilon_f + m_n n_{Bf} + P_f}{(a_1 - 2)(1 + a_2 n_{Bf}^{a_1})} \right]. \quad (18)$$

Alternatively, if the speed of sound is decreasing with increasing density, then we set

$$c_s^2 = a_1 - \frac{a_1 a_2 n_B^{a_1}}{1 + a_2 n_B^{a_1}} \quad (19)$$

and match the boundaries as before ensuring  $\beta \rightarrow 0$  as  $n_B \rightarrow \infty$ . The corresponding energy density is

$$\varepsilon_{NS} = \frac{c_1 n_B {}_2F_1\left(1, -\frac{1}{a_1}, 1 - \frac{1}{a_1}, -\frac{n_B^{-a_1}}{a_2}\right)}{a_2} + c_2 - m_n n_B, \quad (20)$$

where  ${}_2F_1$  is a hypergeometric function with Pfaff's transformation and the constants  $c_1$  and  $c_2$  are

$$c_1 = n_{Bf}^{-a_1-1} (a_2 n_{Bf}^{a_1} + 1) (\varepsilon_f + m_n n_{Bf} + P_f),$$

$$c_2 = n_{Bf}^{-a_1} \left[ a_2 n_{Bf}^{a_1} (\varepsilon_f + m_n n_{Bf}) - (a_2 n_{Bf}^{a_1} + 1) {}_2F_1 \right. \\ \left. \times \left( 1, -\frac{1}{a_1}, 1 - \frac{1}{a_1}, -\frac{n_{Bf}^{-a_1}}{a_2} \right) (\varepsilon_f + m_n n_{Bf} + P_f) \right] \frac{1}{a_2}. \quad (21)$$

Although in practice  $\phi$  is chosen randomly so this is rare, if  $c_s^2(n_{Bf}) = \phi = c_s^2(n_B = 2 \text{ fm}^{-3})$ , then we ensure  $c_s^2$  is constant at high densities. The corresponding energy density is

$$\varepsilon_{NS} = -m_n n_B + \frac{(\varepsilon_f + m_n n_{Bf} + P_f)}{(1 + C_{sf}^2)} \left( \frac{n_B}{n_{Bf}} \right)^{1+C_{sf}^2} \\ + \frac{C_{sf}^2 (\varepsilon_f + m_n n_{Bf}) - P_f}{1 + C_{sf}^2}. \quad (22)$$

This speed of sound correction ensures that neutron star matter is causal, but an additional correction (described below) will be required to ensure that the speed of sound is not larger than the speed of light at all temperatures and electron fractions.

To combine information from QMC near the saturation density and information from neutron star observations at higher densities, we define a function  $h$ ,

$$h = \frac{1}{1 + \exp[\gamma(n_B - \frac{3}{2}n_0)]}, \quad (23)$$

where  $\gamma$  is  $20.0 \text{ fm}^3$ . This function is used to interpolate between the two density regimes.

TABLE I. Skyrme parameters obtained from the chiral EOS used for the finite-temperature corrections in this work.

Parameter	Value
$x_0$	$4.19756 \times 10^1$
$x_1$	$-6.94792 \times 10^{-2}$
$x_2$	$4.19202 \times 10^{-1}$
$x_3$	$-2.87797 \times 10^1$
$t_0$	$5.06729 \times 10^3 \text{ fm}^2$
$t_1$	$1.74925 \text{ fm}^4$
$t_2$	$-4.72119 \times 10^{-1} \text{ fm}^4$
$t_3$	$-1.94596 \times 10^5 \text{ fm}^{2+3\alpha}$
$\alpha$	$1.44165 \times 10^{-1}$

### E. Hot matter near the saturation density

Nuclear two- and three-body forces based on chiral effective theory have shown great progress in computing the EOS of matter near nuclear saturation. The Kohn-Luttinger-Ward perturbation series can be used to compute the EOS of matter at finite temperature as described in Refs. [9,53]. The resulting EOS can then be fitted with a Skyrme interaction, as done for example in Ref. [54]. However, it is difficult to use these results to quantify the uncertainties in these EOS calculations for matter at  $T = 0$  where large cancellations between attractive and repulsive interactions lead to large theoretical errors. We cannot employ the Skyrme interaction from Ref. [54] by itself because this EOS does not necessarily reproduce nuclear structure at  $T = 0$  as does our model which is based on the fit in Ref. [3].

To attempt to address this, we refit only the finite-temperature correction from the chiral EOS,

$$\Delta f_{\text{hot}}(n_B, x_p, T) \equiv f_{\text{hot}}(n_B, x_p, T) - f_{\text{hot}}(n_B, x_p, T = 0), \quad (24)$$

and add these finite temperature corrections on top of our EOS. The EOS for neutron matter ( $x_p = 0$ ) and nuclear matter ( $x_p = 1/2$ ) is obtained from the perturbation series (including the noninteracting contribution) and fitted with a single Skyrme model. The resulting parameter set is given in Table I. We assume that these finite temperature corrections are quadratic in the isospin asymmetry,  $\delta$ . The EOS is not fully quadratic [55,56], but the quadratic approximation is good enough in comparison to the uncertainties in the nature of the strong interaction above the saturation density. We do not expect this Skyrme interaction to give a reasonable description of nuclei or saturated nuclear matter, because we only employ it to describe the finite temperature part of the EOS. There are some regions, especially at large densities, for which the EOS is unstable, i.e.,  $ds/dT < 0$ , but these regions most often result in an acausal EOS and are thus fixed by the speed of sound correction described below.

### F. The full combined EOS

First, we define the symmetry energy to include a zero-temperature contribution which combines the QMC EOS near saturation density, the neutron star fit at higher densities, and

the Skyrme interaction for isospin-symmetric matter:

$$\varepsilon_{\text{sym}}(n_B) = h(n_B)\varepsilon_{\text{QMC}}(n_B) + [1 - h(n_B)]\varepsilon_{\text{NS}}(n_B) - f_{\text{Skyrme}}(n_B, x_p = 1/2, T = 0). \quad (25)$$

Defining the isospin asymmetry  $\delta = 1 - 2x_p$ , we can combine this with the model described above to obtain the free energy density of degenerate matter:

$$f_{\text{deg}}(n_B, x_p, T) = f_{\text{Skyrme}}(n_B, x_p = 1/2, T = 0) + \delta^2 \varepsilon_{\text{sym}}(n_B) + \delta^2 \Delta f_{\text{hot}}(n_B, x_p = 0, T) + (1 - \delta^2) \Delta f_{\text{hot}}(n_B, x_p = 1/2, T). \quad (26)$$

Finally, we ensure that the total nucleonic free energy gives the result from the virial expansion at high temperatures using Eq. (4). When we need to include the electrons, positrons, and photons, we define the free energy density

$$f_{npe\gamma} \equiv f_{np} + f_{e^-} + f_{e^+} + f_{\gamma}. \quad (27)$$

Using this formalism, the chemical potentials and entropy can be computed directly:

$$\begin{aligned} \frac{\partial f_{\text{deg}}}{\partial n_n} &= \frac{1}{2} \mu_{n, \text{Skyrme}}(n_B, x_p = 1/2, T = 0) + \frac{1}{2} \mu_{p, \text{Skyrme}}(n_B, x_p = 1/2, T = 0) + \delta^2 \frac{\partial \varepsilon_{\text{sym}}}{\partial n_B} + \frac{2\delta(1 - \delta)}{n_B} \varepsilon_{\text{sym}} \\ &\quad + \frac{2\delta(1 - \delta)}{n_B} \Delta f_{\text{hot}}(n_B, x_p = 0, T) + \delta^2 \Delta \mu_{n, \text{hot}}(n_B, x_p = 0, T) - \frac{2\delta(1 - \delta)}{n_B} \Delta f_{\text{hot}}(n_B, x_p = 1/2, T) \\ &\quad + (1 - \delta^2) \Delta \mu_{n, \text{hot}}(n_B, x_p = 1/2, T), \end{aligned} \quad (28)$$

$$\begin{aligned} \frac{\partial f_{\text{deg}}}{\partial n_p} &= \frac{1}{2} \mu_{p, \text{Skyrme}}(n_B, x_p = 1/2, T = 0) + \frac{1}{2} \mu_{n, \text{Skyrme}}(n_B, x_p = 1/2, T = 0) + \delta^2 \frac{\partial \varepsilon_{\text{sym}}}{\partial n_B} - \frac{2\delta(1 + \delta)}{n_B} \varepsilon_{\text{sym}} \\ &\quad - \frac{2\delta(1 + \delta)}{n_B} \Delta f_{\text{hot}}(n_B, x_p = 0, T) + \delta^2 \Delta \mu_{p, \text{hot}}(n_B, x_p = 0, T) + \frac{2\delta(1 + \delta)}{n_B} \Delta f_{\text{hot}}(n_B, x_p = 1/2, T) \\ &\quad + (1 - \delta^2) \Delta \mu_{p, \text{hot}}(n_B, x_p = 1/2, T), \end{aligned} \quad (29)$$

and

$$\frac{\partial f_{\text{deg}}}{\partial T} = -\delta^2 s_{\text{hot}}(n_B, x_p = 0, T) - (1 - \delta^2) s_{\text{hot}}(n_B, x_p = 1/2, T), \quad (30)$$

where

$$\begin{aligned} \frac{\partial \varepsilon_{\text{sym}}}{\partial n_B} &= h'(n_B)\varepsilon_{\text{QMC}}(n_B) + h(n_B)\varepsilon'_{\text{QMC}}(n_B) - h'(n_B)\varepsilon_{\text{NS}}(n_B) + [1 - h(n_B)]\varepsilon'_{\text{NS}}(n_B) \\ &\quad - \frac{1}{2} [\mu_{n, \text{Skyrme}}(n_B, x_p = 1/2, T = 0) + \mu_{p, \text{Skyrme}}(n_B, x_p = 1/2, T = 0)]. \end{aligned} \quad (31)$$

In summary, we have five parameters: the values of (i)  $a$  and (ii)  $\alpha$  which determine subsaturation neutron matter, the values of (iii)  $S$  and (iv)  $L$  which determine the symmetry energy and its density dependence, and (v) the value,  $\phi$ , of the speed of sound in neutron star matter at  $n_B = 2 \text{ fm}^{-3}$ . In addition, we have two indices which enumerate random samples from posterior distributions including (i) the index of the Skyrme parametrization from Ref. [3] and (vi) the index of the neutron star EOS from the Markov chain generated in Ref. [51].

### G. Enforcing causality at high density

Since our phenomenological EOS does not have manifest Lorentz covariance, it has the potential to become acausal at high densities. At every electron fraction and temperature, there may be a baryon density,  $n_B^*$ , above which the EOS becomes acausal. Because our phenomenological EOSs (as all other EOS tables) operate as functions of the densities and temperatures, it is useful to rewrite the speed of sound in terms of derivatives of the Helmholtz free energy. This is done in the Appendix below for a general system with any number

of conserved charges (though here we only have two, baryon number and electric charge).

When our phenomenological EOS becomes acausal above some baryon density,  $n_B^*$ , we replace the EOS with a causal EOS,  $\tilde{f}_{\text{C\&P}}$ , following the prescription in Ref. [52]. We construct a modified free energy density with the following:

$$\tilde{f}_{\text{all}} = \tilde{f}_{npe\gamma} \Theta(n_B^* - n_B) + \tilde{f}_{\text{C\&P}} \Theta(n_B - n_B^*), \quad (32)$$

where contributions from electrons, positrons, and photons are included in  $\tilde{f}_{npe\gamma}$ . To be more concise, we suppress the subscripts  $npe\gamma$  in the following. Using  $\varepsilon$  for energy density (including rest mass energy density),  $S$  for entropy,  $s$  for entropy density, and  $\tilde{s}$  for entropy per baryon, the C&P speed of sound is

$$c_s^2 = \left( \frac{dP}{d\varepsilon} \right)_{\tilde{s}, N_B, N_e} = \left( \frac{dP}{d\varepsilon} \right)_{\tilde{s}, N_B, Y_e}. \quad (33)$$

Note that  $\tilde{s} = S/N_B = s/n_B$ , where  $N_B$  is the number of baryons. The C&P derivation begins by noting that

$$P = -\varepsilon + n_B \left( \frac{\partial \varepsilon}{\partial n_B} \right)_{\tilde{s}, N_B, Y_e}. \quad (34)$$

To see this we can write

$$\left(\frac{\partial \varepsilon}{\partial n_B}\right)_{\tilde{s}, N_B, Y_e} = \left[\frac{\partial(E/V)}{\partial V}\right]_{S, N_B, Y_e} \left[\frac{\partial(N_B/V)}{\partial V}\right]_{S, N_B, Y_e}^{-1} = \left(-\frac{P}{V} - \frac{E}{V^2}\right) \left(-\frac{N_B}{V^2}\right)^{-1} = \frac{(P + \varepsilon)}{n_B}. \quad (35)$$

Taking the derivative of Eq. (34), we can also rewrite the pressure as a second derivative:

$$\left(\frac{\partial P}{\partial n_B}\right)_{\tilde{s}, N_B, Y_e} = -\left(\frac{\partial \varepsilon}{\partial n_B}\right)_{\tilde{s}, N_B, Y_e} + \left(\frac{\partial \varepsilon}{\partial n_B}\right)_{\tilde{s}, N_B, Y_e} + n_B \left(\frac{\partial^2 \varepsilon}{\partial n_B^2}\right)_{\tilde{s}, N_B, Y_e} \quad (36)$$

$$= n_B \left(\frac{\partial^2 \varepsilon}{\partial n_B^2}\right)_{\tilde{s}, N_B, Y_e}. \quad (37)$$

Thus we can proceed as C&P do:

$$\left(\frac{\partial^2 \varepsilon}{\partial n_B^2}\right)_{\tilde{s}, N_B, Y_e} - \frac{c_s^2}{n_B} \left(\frac{\partial \varepsilon}{\partial n_B}\right)_{\tilde{s}, N_B, Y_e} = 0. \quad (38)$$

Following the analytical continuation, at every value of  $\tilde{s}$ ,  $N_B$ , and  $Y_e$  in the acausal region, we can use the C&P solution

$$\varepsilon_{\text{C\&P}}(\tilde{s}, n_B, N_B, Y_e) = \left[ \frac{\varepsilon^*(\tilde{s}, N_B, Y_e) + P^*(\tilde{s}, N_B, Y_e)}{\beta + 1} \right] \left[ \frac{n_B}{n_B^*(\tilde{s}, N_B, Y_e)} \right]^{\beta+1} \quad (39)$$

$$+ \left[ \frac{\beta \varepsilon^*(\tilde{s}, N_B, Y_e) - P^*(\tilde{s}, N_B, Y_e)}{\beta + 1} \right]. \quad (40)$$

If we assume that  $\varepsilon^*$ ,  $P^*$ , and  $n_B^*$  are volume independent, then since they are determined at a fixed value of  $n_B$ , they cannot separately depend on  $N_B$ . Thus the full energy density also does not depend on  $N_B$ . To show this explicitly, we start from

$$E = \mu_B N_B + \mu_L N_B Y_e + T S - P V,$$

$$dE = (\mu_B + \mu_L Y_e + T \tilde{s}) dN_B + \mu_L N_B dY_e + T N_B d\tilde{s} - P dV, \quad (41)$$

where  $\mu_L \equiv \mu_p + \mu_e - \mu_n$ . On the right-hand side,

$$dV = \frac{1}{n_B} dN_B - \frac{N_B}{n_B^2} dn_B, \quad (42)$$

and on the left-hand side,

$$dE = d\left(\varepsilon \frac{N_B}{n_B}\right) = \frac{N_B}{n_B} d\varepsilon + \frac{\varepsilon}{n_B} dN_B - \frac{\varepsilon N_B}{n_B^2} dn_B. \quad (43)$$

Substituting the above two equations back into Eq. (41), we find

$$d\varepsilon = \mu_L n_B dY_e + T n_B d\tilde{s} + (\mu_B + \mu_L Y_e + T \tilde{s}) dn_B \quad (44)$$

and the  $N_B$  dependence disappears. Therefore,  $\varepsilon_{\text{C\&P}}(\tilde{s}, n_B, Y_e) = \varepsilon_{\text{C\&P}}(\tilde{s}, n_B, Y_e)$ :

$$\varepsilon_{\text{C\&P}}(\tilde{s}, n_B, Y_e) = \left[ \frac{\varepsilon^*(\tilde{s}, Y_e) + P^*(\tilde{s}, Y_e)}{\beta + 1} \right] \left[ \frac{n_B}{n_B^*(\tilde{s}, Y_e)} \right]^{\beta+1} + \left[ \frac{\beta \varepsilon^*(\tilde{s}, Y_e) - P^*(\tilde{s}, Y_e)}{\beta + 1} \right]. \quad (45)$$

We also find

$$\left(\frac{\partial \varepsilon_{\text{C\&P}}}{\partial Y_e}\right)_{\tilde{s}, n_B} = \mu_L n_B, \quad (46)$$

$$\left(\frac{\partial \varepsilon_{\text{C\&P}}}{\partial \tilde{s}}\right)_{n_B, Y_e} = T n_B, \quad (47)$$

$$\left(\frac{\partial \varepsilon_{\text{C\&P}}}{\partial n_B}\right)_{\tilde{s}, Y_e} = \mu_B + \mu_L Y_e + T \tilde{s}. \quad (48)$$

We choose to use this solution above the value of  $n_B$ , denoted  $n_B^*(\tilde{s}, Y_e)$ , for which  $c_s^2 = \beta$ . From Eq. (47) the temperature is

$$T = \frac{1}{n_B} \left(\frac{\partial \varepsilon_{\text{C\&P}}}{\partial \tilde{s}}\right)_{n_B, Y_e}. \quad (49)$$

Thus computing the temperature using the method in Ref. [52] requires evaluating derivatives of the form  $(\partial n_B^*/\partial \tilde{s})_{Y_e}$ . These derivatives are computed along the surface for which the speed of sound is equal to its largest possible value (which we set to 0.9). Because the speed of sound requires two derivatives of the free energy, these derivatives (derivatives along a line of constant  $c_s^2$ ) require third derivatives of the free energy. The chemical potentials require a similar calculation based on Eqs. (46) and (48) which we do not explicitly show here.

The numerical evaluation of third derivatives introduces quite a bit of noise. Our phenomenological formalism ensures that these derivatives can be computed analytically. We leave this calculation to future work. In the mean time, we can more easily compute the temperature by an indirect approach. Presuming we would like to compute the EOS at some fixed values of the baryon density  $\hat{n}_B$ , electron fraction  $\hat{Y}_e$ , and temperature  $\hat{T}$ , one needs to solve the five equations

$$\begin{aligned} c_{s, \text{DS}}^2(n_{B1}^*, \hat{Y}_e, T_1^*) &= \beta, \\ c_{s, \text{DS}}^2(n_{B2}^*, \hat{Y}_e, T_2^*) &= \beta, \\ \tilde{s}_{\text{DS}}(n_{B1}^*, \hat{Y}_e, T_1^*) &= \tilde{s}, \\ \tilde{s}_{\text{DS}}(n_{B2}^*, \hat{Y}_e, T_2^*) &= \tilde{s} + \delta \tilde{s}, \\ \frac{1}{\hat{n}_B} \frac{\varepsilon_{\text{C\&P}}(\tilde{s} + \delta \tilde{s}, \hat{Y}_e, n_B) - \varepsilon_{\text{C\&P}}(\tilde{s}, \hat{Y}_e, n_B)}{\delta \tilde{s}} &= \hat{T} \end{aligned} \quad (50)$$

for the five values  $n_{B1}^*$ ,  $n_{B2}^*$ ,  $T_1^*$ ,  $T_2^*$ , and  $\tilde{s}$  given some small fixed step size in the entropy per baryon,  $\delta \tilde{s}$ . Here “DS” denotes our EOS while “C&P” denotes Eq. (39) from Ref. [52]. The required numerical derivatives to compute the temperature in the last equation of Eqs. (50) can then be computed directly from finite differences. By solving the five equations above, we get  $\tilde{s}_{\text{C\&P}}(\hat{n}_B, \hat{Y}_e, \hat{T})$ , and then

$$\tilde{f}_{\text{C\&P}}(\hat{n}_B, \hat{Y}_e, \hat{T}) = \varepsilon_{\text{C\&P}} - \hat{T} \hat{n}_B \tilde{s}_{\text{C\&P}}(\hat{n}_B, \hat{Y}_e, \hat{T}). \quad (51)$$

### III. RESULTS

Figure 2 shows how our full EOS behaves in (i) the nondegenerate limit, (ii) the limit of zero-temperature neutron matter, and (iii) the limit of high-temperature and high-density nuclear matter. Only one parameter set is chosen and the same parameter set is chosen for each of the three panels. In the

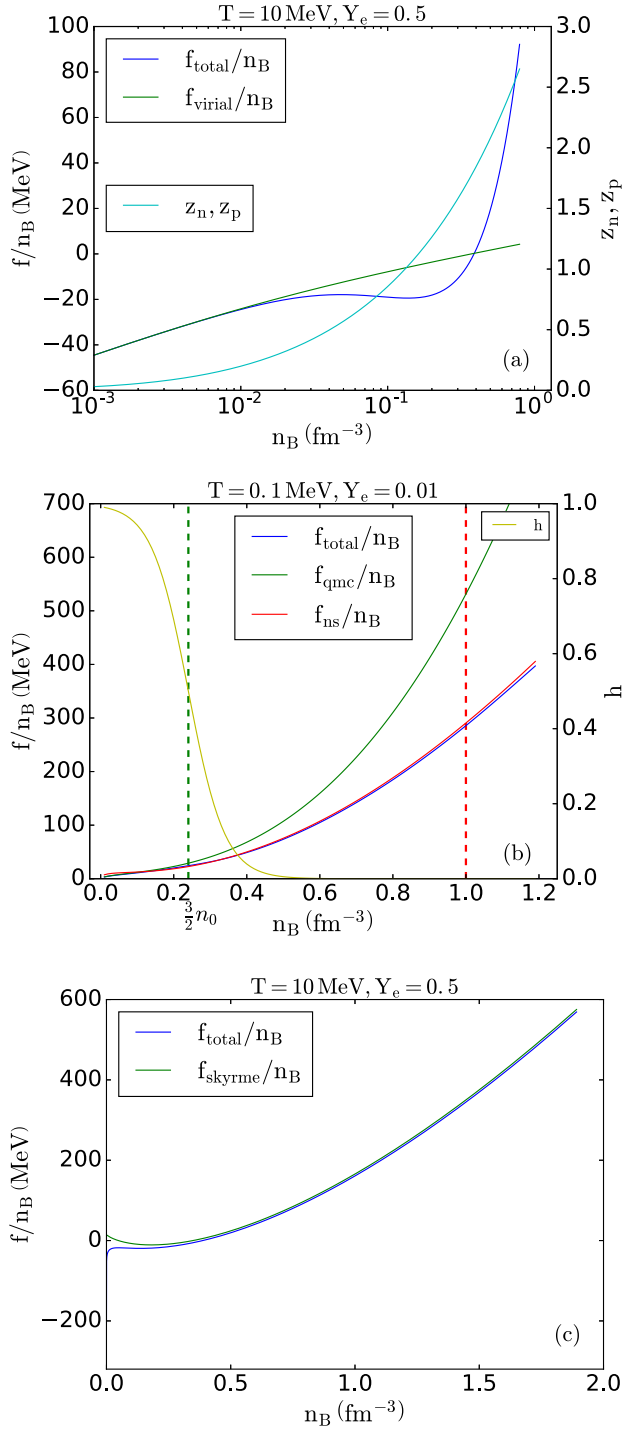


FIG. 2. Three figures which show how the full EOS compares to the limiting forms. The top panel compares the full free energy to the result from the virial expansion and shows that they match at lower densities where the fugacities are much smaller than 1. The middle panel shows that the result for neutron matter matches the QMC free energy at low densities, the neutron star free energy at densities reached in the neutron star interiors, and is softened at high densities to ensure a speed of sound less than the speed of light. The bottom panel shows that free energy starts to deviate from the Skyrme interaction at higher temperatures as the corrections from the chiral EOS begin to contribute. These panels show the result from one of many EOSs generated in this work.

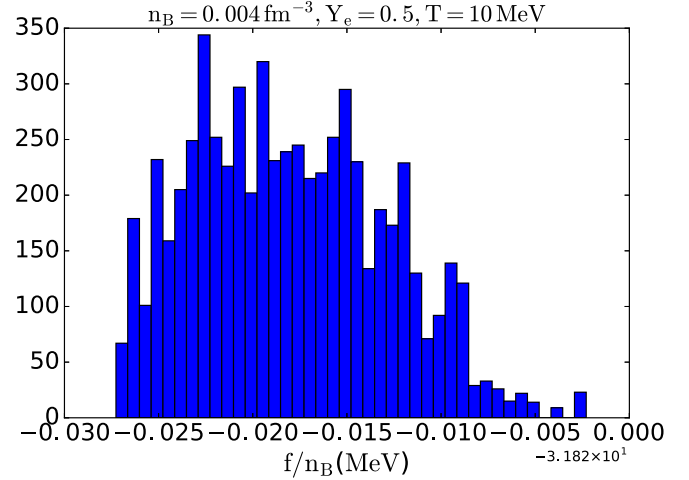


FIG. 3. The probability distribution for the free energy per baryon at  $n_B = 0.004$  fm $^{-3}$ ,  $Y_e = 0.5$ , and  $T = 10$  MeV.

nondegenerate limit, our full EOS smoothly matches on to the virial EOS as determined by Eq. (5). The middle panel shows that, in the limit of zero-temperature neutron matter, our full EOS matches the QMC result at low density and remains close to the neutron star EOS at moderate densities. At higher densities, the free energy does not increase too quickly with density because our correction for causality begins to start becoming important. The bottom panel compares our full EOS (for this parametrization) with the ( $T = 0$ ) Skyrme EOS, showing a small modification in the EOS due to the finite temperature correction from the chiral EOS.

We can construct a figure similar to Fig. 2 for any physical combination of our model parameters:  $\alpha$ ,  $a$ ,  $S$ ,  $L$ ,  $\phi$ , and the Skyrme model from Ref. [3] (which represents a 12-dimensional space of possible Skyrme models) and any neutron star model from Ref. [51] (which represents a six-dimensional space of high-density EOSs).

For any baryon density, electron fraction, and temperature, we can compute a probability distribution for the free energy per baryon over our entire parameter space. The magnitude and shape of the uncertainty in the free energy changes depending on the relevant physics in that region which our model describes. Figure 3 shows the variation in the free energy in nondegenerate matter where the EOS is dominated by the virial expansion. The small remaining uncertainty here originates in the Skyrme model that is selected, and the nonsmooth nature in the probability distribution is a relic of the limited sampling size of Skyrme interactions.

Figure 4 shows the variation in the free energy per baryon at nuclear saturation density in nearly pure neutron matter and in the limit of zero temperature. The results for LS220, SFHo, SFHx, and IUFSU are also shown. The distribution is centered around 16 MeV, corresponding to a symmetry energy of 32 MeV, and values lower than 13 MeV are excluded from our model because they correspond to symmetry energies lower than 29.5 MeV. Symmetry energies this small seem to be excluded from quantum Monte Carlo and chiral effective field theory calculations of pure neutron matter [21,47,57].



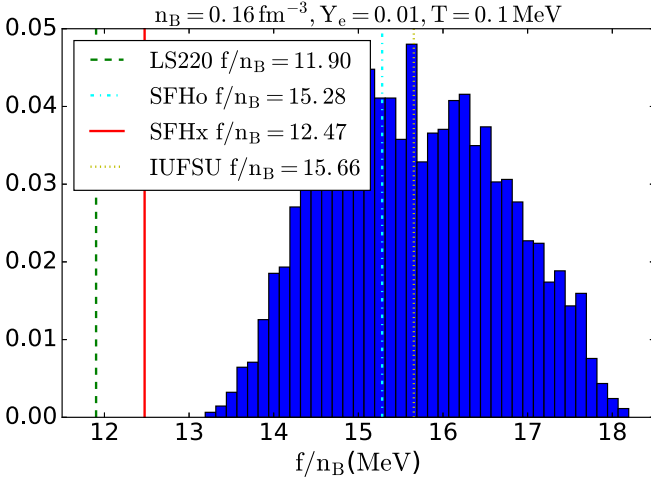


FIG. 4. The probability distribution for the free energy per baryon at  $n_B = 0.16 \text{ fm}^{-3}$ ,  $Y_e = 0.01$ , and  $T = 0.1 \text{ MeV}$ .

See also Ref. [22] for a more general result that gives a similar lower limit for  $S$  of 28 MeV.

Figure 5 shows the distribution in the free energy per baryon at a slightly larger temperature, and the entropy contribution drops the free energy per baryon in each case. In comparison to the results from Fig. 4, the LS220 free energy per particle drops more than SFHo or SFHx because its effective mass (equal to the nucleon mass) is larger than that in SFHo/x (about 0.7 times the nucleon mass). The effective mass can be computed from the chiral interaction directly [58,59], and close to the Fermi surface it is found to be nearly equal to the free-space nucleon mass. Second-order many-body perturbation theory contributions, however, produce a strong momentum dependence in this region, and averaging around  $k = k_F$  the effective mass is about 0.85 times the free-space nucleon mass. The distribution in Fig. 5 is thus larger than LS220 because of the smaller symmetry energy ( $S = 28.6 \text{ MeV}$ ) and larger effective mass in the LS220 EOS.

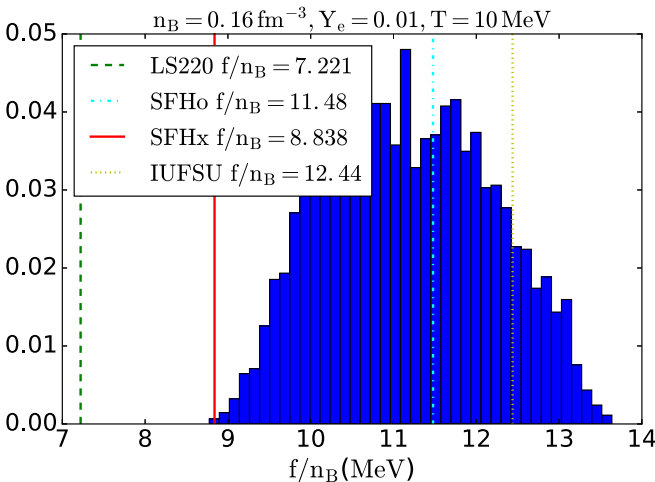


FIG. 5. The probability distribution for the free energy per baryon at  $n_B = 0.16 \text{ fm}^{-3}$ ,  $Y_e = 0.01$ , and  $T = 10 \text{ MeV}$ .

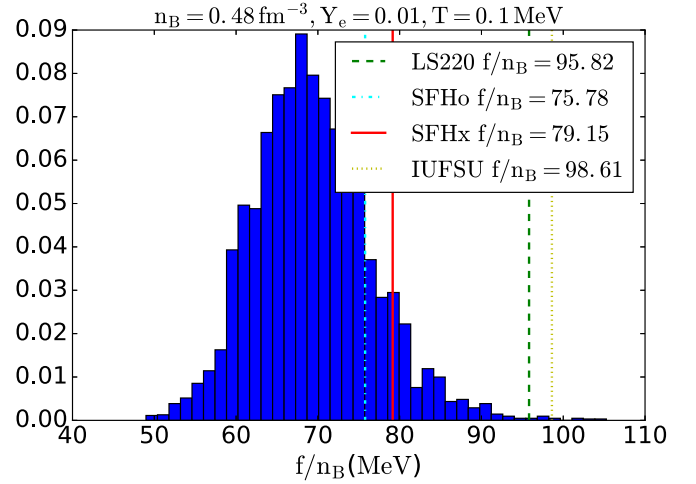


FIG. 6. The probability distribution for the free energy per baryon at  $n_B = 0.48 \text{ fm}^{-3}$ ,  $Y_e = 0.10$ , and  $T = 0.1 \text{ MeV}$ .

Figure 6 shows the probability distribution for the low-temperature neutron-rich matter free energy per baryon at higher densities. There is clearly a much larger spread in the free energy per baryon, corresponding to our larger ignorance regarding the nature of matter at higher density. While all models LS220, SFHo, SFHx, and IUFSU are inside the region suggested by our parametrization, our distribution leans towards smaller values of the free energy because of the constraint from relatively small neutron star radii.

Figure 7 shows low-temperature nuclear matter at higher densities. The nonsmooth nature of the distribution is due to the small statistics afforded by the limited number of Skyrme models we have employed. IUFSU suggests a larger free energy here because it originates in a relativistic mean field model which tends to give larger pressures than the nonrelativistic models like Skyrme. This region of parameter space is almost entirely unconstrained by experiment, since it is not possible to make cold isospin-symmetric matter at this

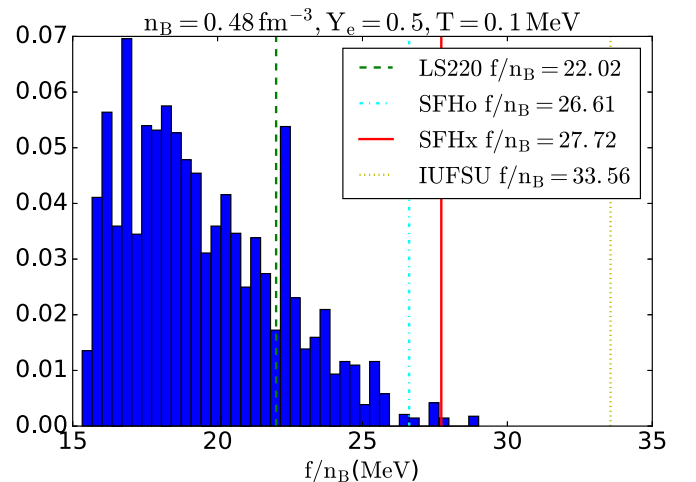


FIG. 7. The probability distribution for the free energy per baryon at  $n_B = 0.48 \text{ fm}^{-3}$ ,  $Y_e = 0.5$ , and  $T = 0.1 \text{ MeV}$ .

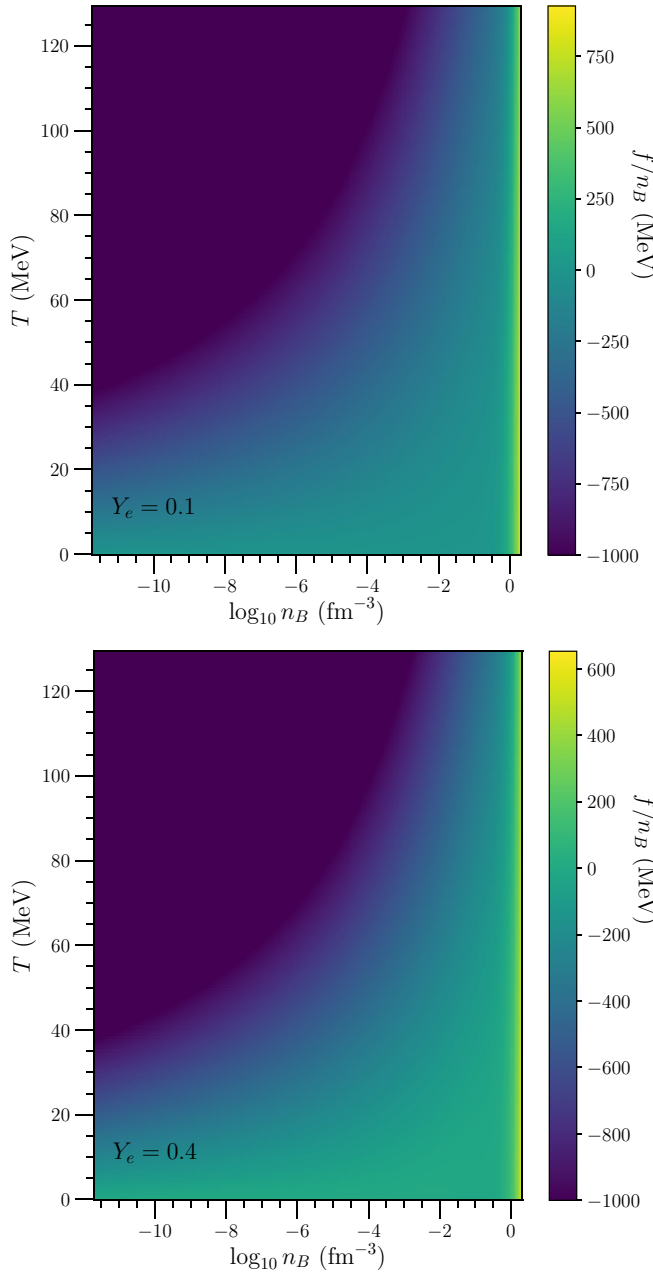


FIG. 8. Density plots showing the free energy per baryon for matter at  $Y_e = 0.1$  and  $Y_e = 0.4$  over the full range of densities and temperatures considered in this work for one parametrization. Points with a free energy per baryon less than  $-1000$  MeV are set equal to  $-1000$  MeV to make the high-density behavior more clear. The main variation in the free energy per baryon from the lower-right region to the upper-left region in these plots is dominated by the virial contribution to the EOS. The degenerate part of the EOS is clear in the large increase in the free energy per baryon on the right-hand boundary (at large baryon densities).

density. However, dense isospin-symmetric matter is not as relevant for this work since simulations are typically neutron rich at high density.

Figure 8 shows the free energy per baryon for one of our parametrizations as a function of baryon density and

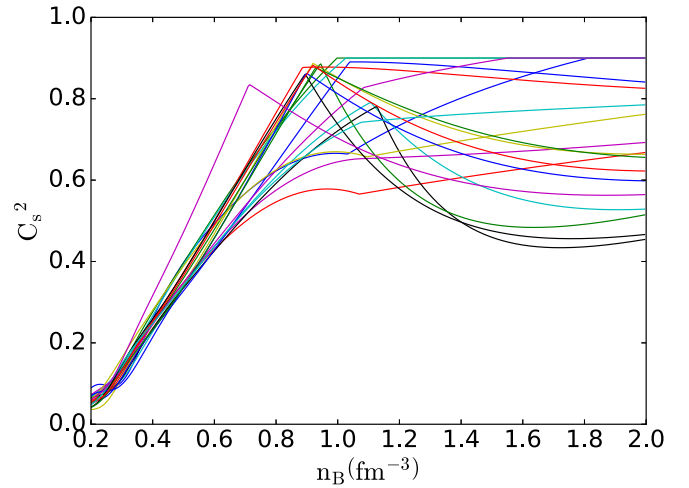


FIG. 9. Values of  $n_B$  and  $c_s^2$  explored by the EOS at  $Y_e = 0.1$  and  $\tilde{s} = 0.5$ . The different curves represent models which differ only by a different value of the parameter  $\phi$ .

temperature for two electron fractions. Using the formalism presented in this work, thousands of similar density plots can be generated with alternate parametrizations. The largest variation between parametrizations is in the free energy per particle at high density which changes with the “stiffness” of the EOS.

Since accurate neutron star radii have not yet been measured for large mass neutron stars, the speed of sound of matter at the highest densities probed in supernova and merger simulations is not constrained by experiment. We have parametrized this variation with  $\phi$ . However, the speed of sound must increase at moderate densities in order to reproduce the observation of a two-solar-mass neutron star. Figure 9 shows the behavior of the speed of sound in neutron-rich matter between  $n_B = 0.1 \text{ fm}^{-3}$  and  $n_B = 2 \text{ fm}^{-3}$  and demonstrates these two regimes. The speed of sound must increase quickly below  $1 \text{ fm}^{-3}$  to ensure that the neutron star maximum mass is sufficiently large [60], and the speed of sound at higher densities varies considerably depending on the value of  $\phi$ . We restrict the speed of sound to be less than  $c\sqrt{0.9}$  to ensure finite-precision errors in simulations do not create unphysical sound speeds.

In high-density isospin-symmetric matter, the speed of sound is dominated by the Skyrme model used for isospin-symmetric matter near the saturation density. This region is principally constrained to have a speed of sound less than  $c\sqrt{0.9}$  by our implementation of the prescription from Ref. [52] as described in Sec. II G. This is shown in Fig. 10. There is also a slight residual impact from the modification in the speed of sound from  $\phi$  at values of  $Y_e$  which are nearly but not exactly equal to  $1/2$ , so there are some slight kinks in the curves in Fig. 10 near  $n_B = 1 \text{ fm}^{-3}$ .

At sufficiently high density, the entropy from the chiral EOS begins decreasing with increasing temperature. Because of the presence of  $ds/dT$  in the speed of sound [see  $f_{TT}$  in the denominator of Eq. (A12)], this unstable region implies a large speed of sound. Our use of the C&P prescription thus

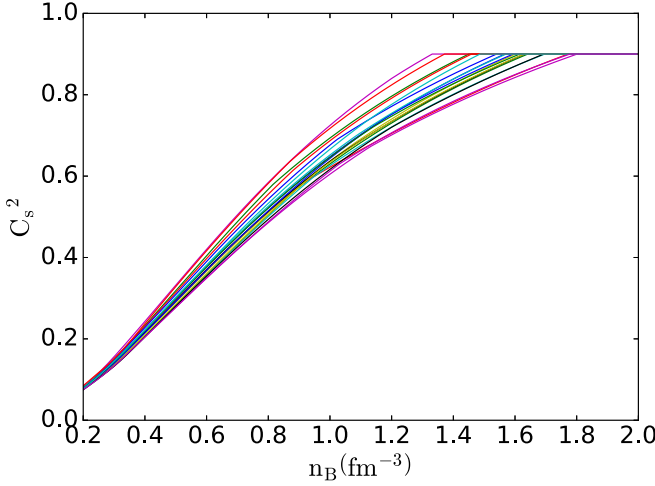


FIG. 10. Values of  $n_B$  and  $c_s^2$  explored by the EOS at  $Y_e = 0.4$  and  $\tilde{s} = 0.5$ . The different curves represent randomly selected models. Most of them have two kinks. The first one (often very slight) is the residual impact of fixing the speed of sound in neutron matter at high densities to  $\phi$  as shown in Fig. 9. The second kink between  $1.3 < n_B^* < 1.8 \text{ fm}^{-3}$  is due to the use of the C&P prescription to decrease the speed of sound above  $n_B = n_B^*$ .

cures this instability in the extrapolated form of the finite-temperature corrections from the chiral EOS. This is demonstrated in Fig. 11, which shows contours of fixed  $ds/dT$ . This derivative becomes negative in the upper right region, but this

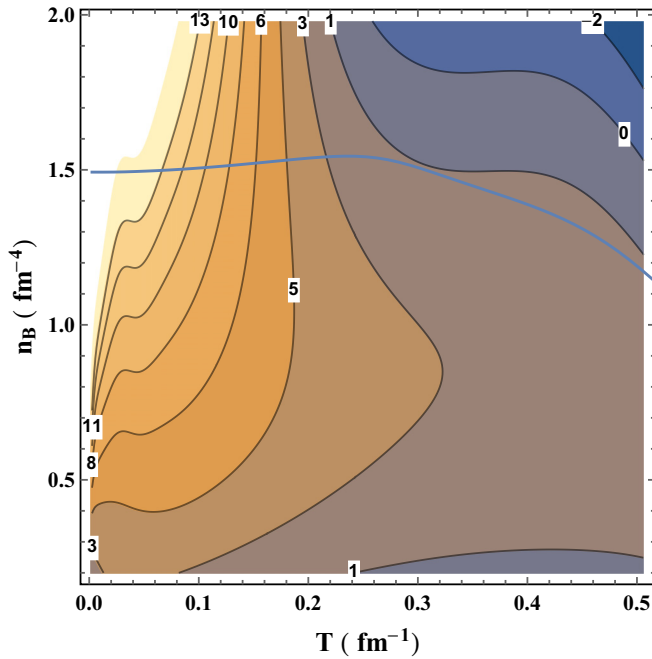


FIG. 11. Contour plot of  $ds/dT$  as a function of  $n_B$  and  $T$  explored by the EOS for one of our EOS parametrizations. The speed of sound correction from the C&P prescription has not yet been applied. The blue line indicates the value  $n_B = n_B^*$ . The region above this line is replaced with the C&P EOS (including the region where  $ds/dT < 0$ ).

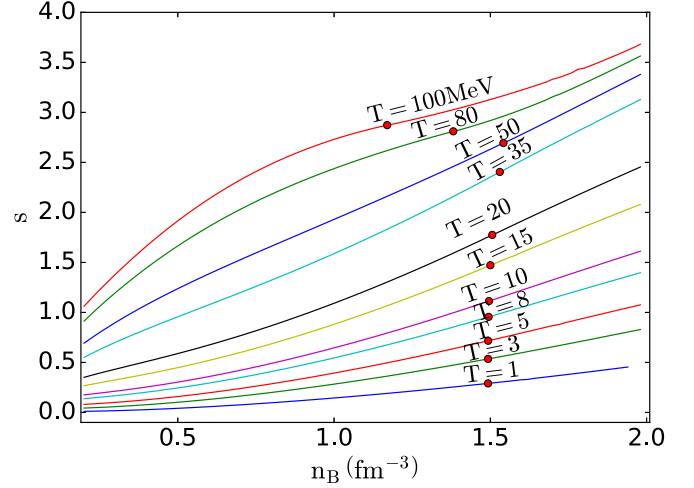


FIG. 12. Values of  $n_B$  and  $s$  explored by the EOS. The dots represent boundaries where  $c_s^2 = 0.9$  and the C&P solution starts to take effect.

is always at a density larger than  $n_B^*$  where the C&P EOS takes over.

As a final demonstration that our implementation of the C&P prescription generates a continuous EOS, we show the entropy as a function of density for several fixed temperatures in Fig. 12. Our EOS above is used for densities below  $n_B^*$  (indicated by the red dot) and the C&P EOS is used for densities above  $n_B^*$ . It appears in this plot that  $n_B^*$  is independent of temperature, but this is not exactly true as there is a weak temperature dependence as shown in Fig. 11. We have found that solving Eqs. (50) is numerically challenging because of the numerical derivatives involved in computing the speed of sound (we use exact expressions for the entropy and chemical potentials but numerical differentiation for the number susceptibilities and other second derivatives of the free energy). The combination of the numerical derivatives plus the numerical noise in the Newton-Raphson method used to solve Eqs. (50) leads to a bit of noise in the entropy at large densities. Future work will use exact expressions for second derivatives of the free energy and thus facilitate the correction to the speed of sound.

#### IV. DISCUSSION

While we have made an attempt to explore the allowed EOS space as much as possible, there are several regions in which our parametrization is limited. Variations in the functions  $g$  and  $h$  could be explored, but modifications of these functions cannot be too large or they are likely to create small regions where the EOS has an acausal speed of sound. A better quantification of the uncertainties in the finite temperature part of the chiral EOS will be performed in future work. We have also naively extrapolated the Skyrme model used in isospin-symmetric matter at zero temperature near the saturation density to higher densities. There is some experimental constraint on matter in this region from heavy ion collisions [61], but the associated systematic uncertainties are not well understood. In any case, dense and isospin-symmetric matter

is not often explored in the neutron-rich matter encountered in neutron stars.

Uncertainties in the EOS may be relevant for the timescale for core-collapse supernovas to explode after bounce [62] and also, for example, in determining the amount of r-process nucleosynthesis which occurs in the neutrino-driven wind [63]. EOS uncertainties are also relevant for neutron star mergers, as they dictate the lifetime of hypermassive neutron star remnants and also the amount of r-process material ejected [64].

Because we use the Markov chain from “Model A” in Ref. [51], our EOS specifically prefers more moderate phase transitions, which is appropriate to our assumption that matter consists only of nucleons and no exotic matter. Thus our uncertainties at high density may be underestimated because strong phase transitions are disfavored. One of the advantages of our analytical form for the EOS is that our work can be easily generalized to an EOS which includes exotic matter at high densities if desired.

This article is the first step towards a full quantification of how microphysical uncertainties may affect core-collapse supernovas and neutron star mergers. The next step is a full description of nuclei in the dense matter environment with uncertainties that properly reflect the relationship between nuclear structure and the underlying nucleon-nucleon interaction. One way to include nuclei on top of our EOS for homogeneous matter is to use the framework recently

developed in Ref. [65]. Finally, the EOS uncertainties must be propagated through to the neutrino opacities. As this uncertainty quantification matures, the comparison of simulations with data points, such as GW170817 [66] and future nearby core-collapse supernovas, will provide more insight into what models might be ruled out.

## ACKNOWLEDGMENTS

The authors would like to thank D. Higdon for supplying the samples from the posterior generated in Ref. [3]. X.D. and A.W.S. were supported by DOE SciDAC Grant No. DE-SC0018232 and NSF Grant No. PHY 1554876, and J.W.H. was supported by NSF Grant No. PHY 1652199. Portions of this research were conducted with the advanced computing resources provided by Texas A&M High Performance Research Computing.

## APPENDIX: SPEED OF SOUND FOR A MULTICOMPONENT SYSTEM

Using  $\varepsilon$  for energy density,  $S$  for entropy,  $s$  for entropy density, and  $\bar{s}$  for entropy per baryon, and assuming neutrinos are not trapped, the speed of sound is (all chemical potentials and energy densities below include the rest mass contribution even though not explicitly indicated)

$$c_s^2 = \left( \frac{\partial P}{\partial \varepsilon} \right)_{\bar{s}, \{N_i\}}. \quad (\text{A1})$$

In infinite matter, it is useful to rewrite this derivative in terms of fixed volume rather than fixed number:

$$c_s^2 = \left( \frac{\partial P}{\partial \varepsilon} \right)_{S, \{N_i\}} = \left( \frac{\partial P}{\partial V} \right)_{S, \{N_i\}} \left( \frac{\partial \varepsilon}{\partial V} \right)_{S, \{N_i\}}^{-1}, \quad (\text{A2})$$

where the second derivative on the right-hand side of this expression is

$$\left( \frac{\partial \varepsilon}{\partial V} \right)_{S, \{N_i\}} = \left[ \frac{\partial (E/V)}{\partial V} \right]_{S, \{N_i\}} = -\frac{1}{V}P - \frac{E}{V^2} = -\frac{P + \varepsilon}{V} = -\frac{Ts + \sum_i \mu_i n_i}{V} \quad (\text{A3})$$

and the first derivative on the right-hand side is

$$\left( \frac{\partial P}{\partial V} \right)_{S, \{N_j\}} = -\left( \frac{\partial \varepsilon}{\partial V} \right)_{S, \{N_j\}} + S \left[ \frac{\partial (T/V)}{\partial V} \right]_{S, \{N_j\}} + \sum_i N_i \left[ \frac{\partial (\mu_i/V)}{\partial V} \right]_{S, \{N_j\}} \quad (\text{A4})$$

$$= -\left( \frac{\partial \varepsilon}{\partial V} \right)_{S, \{N_j\}} + S \left[ -\frac{T}{V^2} + \left( \frac{\partial T}{\partial V} \right)_{S, \{N_j\}} \right] + \sum_i N_i \left[ -\frac{\mu_i}{V^2} + \left( \frac{\partial \mu_i}{\partial V} \right)_{S, \{N_j\}} \right] \quad (\text{A5})$$

$$= \frac{P + \varepsilon}{V} + S \left[ -\frac{T}{V^2} - \left( \frac{\partial P}{\partial S} \right)_{\{N_j\}, V} \right] + \sum_i N_i \left[ -\frac{\mu_i}{V^2} - \left( \frac{\partial P}{\partial N_i} \right)_{S, \{N_{j \neq i}\}, V} \right] \\ = -S \left( \frac{\partial P}{\partial S} \right)_{\{n_j\}, V} - \sum_i N_i \left( \frac{\partial P}{\partial N_i} \right)_{S, \{n_{j \neq i}\}, V}. \quad (\text{A6})$$

Putting these two results together gives

$$c_s^2 = \left[ s \left( \frac{\partial P}{\partial S} \right)_{\{n_j\}, V} + \sum_i n_i \left( \frac{\partial P}{\partial n_i} \right)_{S, \{n_{j \neq i}\}, V} \right] \left( Ts + \sum_i \mu_i n_i \right)^{-1}. \quad (\text{A7})$$



To reexpress this in terms of derivatives of the free energy,

$$c_s^2 = \left\{ s \left[ \frac{\partial (\sum_i \mu_i n_i - f)}{\partial s} \right]_{\{n_j\}, V} + \sum_i n_i \left[ \frac{\partial (\sum_k \mu_k n_k - f)}{\partial n_i} \right]_{s, \{n_{j \neq i}\}, V} \right\} \left( Ts + \sum_i \mu_i n_i \right)^{-1}. \quad (\text{A8})$$

For the sum over  $k$ , all densities are constant except for  $n_i$ ; thus

$$\begin{aligned} \sum_i n_i \frac{\partial}{\partial n_i} \left( \sum_k \mu_k n_k - f \right)_{s, \{n_{j \neq i}\}, V} &= \sum_i n_i \frac{\partial}{\partial n_i} \left( \sum_{k \neq i} \mu_k n_k + \mu_i n_i - f \right)_{s, \{n_{j \neq i}\}, V} \\ &= \sum_i \left[ \sum_k n_k \left( \frac{\partial \mu_k}{\partial n_i} \right)_{s, \{n_{j \neq i}\}, V} + \mu_i - \left( \frac{\partial f}{\partial n_i} \right)_{s, \{n_{j \neq i}\}, V} \right]. \end{aligned} \quad (\text{A9})$$

To compute this we need

$$\begin{aligned} \left( \frac{\partial f}{\partial n_i} \right)_{s, \{n_{j \neq i}\}, V} &= \left( \frac{\partial f}{\partial n_i} \right)_{\{n_{j \neq i}\}, T, V} + \left( \frac{\partial f}{\partial T} \right)_{n_B, \{n_{j \neq i}\}, V} \left( \frac{\partial T}{\partial n_i} \right)_{\{n_{j \neq i}\}, s, V} = \mu_i - s \left( \frac{\partial T}{\partial n_i} \right)_{\{n_{j \neq i}\}, s, V}, \\ \left( \frac{\partial \mu_k}{\partial n_i} \right)_{s, \{n_{j \neq i}\}, V} &= \left( \frac{\partial \mu_k}{\partial n_i} \right)_{\{n_{j \neq i}\}, T, V} + \left( \frac{\partial \mu_k}{\partial T} \right)_{n_i, \{n_{j \neq i}\}, V} \left( \frac{\partial T}{\partial n_i} \right)_{\{n_{j \neq i}\}, s, V} = f_{n_i n_k} + f_{n_k T} \left( \frac{\partial T}{\partial n_i} \right)_{\{n_{j \neq i}\}, s, V}, \end{aligned} \quad (\text{A10})$$

which requires

$$\left( \frac{\partial T}{\partial n_i} \right)_{\{n_{j \neq i}\}, s, V} = - \left( \frac{\partial s}{\partial n_i} \right)_{\{n_{j \neq i}\}, T, V} \left( \frac{\partial s}{\partial T} \right)_{\{n\}, V}^{-1} = -f_{n_i T} / f_{TT}. \quad (\text{A11})$$

Finally, we get

$$\begin{aligned} c_s^2 &= \left\{ - \left( \frac{s}{f_{TT}} \right) \left( \sum_i n_i f_{n_i T} + s \right) + \sum_i n_i \left[ \sum_k n_k (f_{n_i n_k} - f_{n_k T} f_{n_i T} f_{TT}^{-1}) - s f_{n_i T} f_{TT}^{-1} \right] \right\} \left( Ts + \sum_i \mu_i n_i \right)^{-1} \\ &= \left[ \sum_i \sum_k n_i n_k (f_{n_i n_k} - f_{n_k T} f_{n_i T} f_{TT}^{-1}) - 2 \sum_i s n_i f_{n_i T} f_{TT}^{-1} - s^2 f_{TT}^{-1} \right] \left( Ts + \sum_i \mu_i n_i \right)^{-1}. \end{aligned} \quad (\text{A12})$$

- 
- [1] W. R. Hix, E. J. Lentz, E. Endeve, M. Baird, M. A. Chertkow, J. A. Harris, O. E. B. Messer, A. Mezzacappa, S. Bruenn, and J. Blondin, *AIP Adv.* **4**, 041013 (2014).
- [2] L. Baiotti and L. Rezzolla, *Rep. Prog. Phys.* **80**, 096901 (2017).
- [3] M. Kortelainen, J. McDonnell, W. Nazarewicz, E. Olsen, P.-G. Reinhard, J. Sarich, N. Schunck, S. M. Wild, D. Davesne, J. Erler, and A. Pastore, *Phys. Rev. C* **89**, 054314 (2014).
- [4] X. Roca-Maza, N. Paar, and G. Colo, *J. Phys. G* **42**, 034033 (2015).
- [5] S. Gandolfi, A. Gezerlis, and J. Carlson, *Annu. Rev. Nucl. Part. Sci.* **65**, 303 (2015).
- [6] K. Hebeler, J. D. Holt, J. Menendez, and A. Schwenk, *Annu. Rev. Nucl. Part. Sci.* **65**, 457 (2015).
- [7] L. Coraggio, J. W. Holt, N. Itaco, R. Machleidt, and F. Sammarruca, *Phys. Rev. C* **87**, 014322 (2013).
- [8] A. Mukherjee and V. R. Pandharipande, *Phys. Rev. C* **75**, 035802 (2007).
- [9] C. Wellenhofer, J. W. Holt, and N. Kaiser, *Phys. Rev. C* **92**, 015801 (2015).
- [10] A. Carbone, A. Cipollone, C. Barbieri, A. Rios, and A. Polls, *Phys. Rev. C* **88**, 054326 (2013).
- [11] C. Drischler, K. Hebeler, and A. Schwenk, *Phys. Rev. C* **93**, 054314 (2016).
- [12] C. J. Horowitz and A. Schwenk, *Phys. Lett. B* **638**, 153 (2006).
- [13] C. J. Horowitz and A. Schwenk, *Nucl. Phys. A* **776**, 55 (2006).
- [14] P. Demorest, T. Pennucci, S. Ransom, M. Roberts, and J. W. T. Hessels, *Nature (London)* **467**, 1081 (2010).
- [15] J. Antoniadis *et al.*, *Science* **340**, 1233232 (2013).
- [16] J. M. Lattimer and F. D. Swesty, *Nucl. Phys. A* **535**, 331 (1991).
- [17] D. H. Youngblood, H. L. Clark, and Y.-W. Lui, *Phys. Rev. Lett.* **82**, 691 (1999).
- [18] S. Shlomo, V. M. Kolomietz, and G. Colò, *Eur. Phys. J. A* **30**, 23 (2006).
- [19] T. Fischer, M. Hempel, I. Sagert, Y. Suwa, and J. Schaffner-Bielich, *Eur. Phys. J. A* **50**, 46 (2014).
- [20] J. M. Lattimer and A. W. Steiner, *Eur. Phys. J. A* **50**, 40 (2014).
- [21] J. W. Holt and N. Kaiser, *Phys. Rev. C* **95**, 034326 (2017).
- [22] I. Tews, J. M. Lattimer, A. Ohnishi, and E. E. Kolomeitsev, *Astrophys. J.* **848**, 105 (2017).
- [23] H. Shen, H. Toki, K. Oyamatsu, and K. Sumiyoshi, *Nucl. Phys. A* **637**, 435 (1998).
- [24] A. W. Steiner, J. M. Lattimer, and E. F. Brown, *Astrophys. J.* **722**, 33 (2010).
- [25] K. Hebeler, J. M. Lattimer, C. J. Pethick, and A. Schwenk, *Phys. Rev. Lett.* **105**, 161102 (2010).
- [26] A. Burrows and J. M. Lattimer, *Astrophys. J.* **285**, 294 (1984).

- [27] W. R. Hix, O. E. B. Messer, A. Mezzacappa, M. Liebendörfer, J. Sampaio, K. Langanke, D. J. Dean, and G. Martinez-Pinedo, *Phys. Rev. Lett.* **91**, 201102 (2003).
- [28] A. S. Botvina and I. N. Mishustin, *Phys. Rev. C* **72**, 048801 (2005).
- [29] E. O'Connor, D. Gazit, C. J. Horowitz, A. Schwenk, and N. Barnea, *Phys. Rev. C* **75**, 055803 (2007).
- [30] A. Arcones, G. Martinez-Pinedo, E. O'Connor, A. Schwenk, H.-T. Janka, C. J. Horowitz, and K. Langanke, *Phys. Rev. C* **78**, 015806 (2008).
- [31] S. R. Souza, A. W. Steiner, W. G. Lynch, R. Donangelo, and M. A. Famiano, *Astrophys. J.* **707**, 1495 (2009).
- [32] G. Shen, C. J. Horowitz, and S. Teige, *Phys. Rev. C* **82**, 045802 (2010).
- [33] B. G. Todd-Rutel and J. Piekarewicz, *Phys. Rev. Lett.* **95**, 122501 (2005).
- [34] M. Hempel, T. Fischer, J. Schaffner-Bielich, and M. Liebendörfer, *Astrophys. J.* **748**, 70 (2012).
- [35] S. Typel, G. Röpke, T. Klähn, D. Blaschke, and H. H. Wolter, *Phys. Rev. C* **81**, 015803 (2010).
- [36] F. J. Fattoyev, C. J. Horowitz, J. Piekarewicz, and G. Shen, *Phys. Rev. C* **82**, 055803 (2010).
- [37] A. W. Steiner, M. Hempel, and T. Fischer, *Astrophys. J.* **774**, 17 (2013).
- [38] S. Typel, M. Oertel, and T. Klähn, *Phys. Part. Nucl.* **46**, 633 (2015); <http://compose.obspm.fr/>
- [39] S. Banik, M. Hempel, and D. Bandyopadhyay, *Astrophys. J. Suppl. Ser.* **214**, 22 (2014).
- [40] M. Prakash, T. L. Ainsworth, and J. M. Lattimer, *Phys. Rev. Lett.* **61**, 2518 (1988).
- [41] M. Oertel, M. Hempel, T. Klähn, and S. Typel, *Rev. Mod. Phys.* **89**, 015007 (2017).
- [42] G. Shen, C. J. Horowitz, and E. O'Connor, *Phys. Rev. C* **83**, 065808 (2011).
- [43] C. J. Horowitz, G. Shen, E. O'Connor, and C. D. Ott, *Phys. Rev. C* **86**, 065806 (2012).
- [44] A. Gårdestig, *J. Phys. G: Nucl. Part. Phys.* **36**, 053001 (2009).
- [45] M. P. Valderrama and E. R. Arriola, *Phys. Rev. C* **72**, 044007 (2005).
- [46] R. Navarro Perez, N. Schunck, A. Dyhdalo, R. J. Furnstahl, and S. K. Bogner, *Phys. Rev. C* **97**, 054304 (2018).
- [47] S. Gandolfi, J. Carlson, and S. Reddy, *Phys. Rev. C* **85**, 032801 (2012).
- [48] T. Krüger, I. Tews, K. Hebeler, and A. Schwenk, *Phys. Rev. C* **88**, 025802 (2013).
- [49] E. Chabanat, P. Bonche, P. Haensel, J. Meyer, and R. Schaeffer, *Phys. Scr.* **T56**, 231 (1995).
- [50] A. W. Steiner, M. Prakash, J. M. Lattimer, and P. J. Ellis, *Phys. Rep.* **411**, 325 (2005).
- [51] A. W. Steiner, S. Gandolfi, F. J. Fattoyev, and W. G. Newton, *Phys. Rev. C* **91**, 015804 (2015).
- [52] C. Constantinou and M. Prakash, *Phys. Rev. C* **95**, 055802 (2017).
- [53] C. Wellenhofer, J. W. Holt, N. Kaiser, and W. Weise, *Phys. Rev. C* **89**, 064009 (2014).
- [54] Y. Lim and J. W. Holt, *Phys. Rev. C* **95**, 065805 (2017).
- [55] A. W. Steiner, *Phys. Rev. C* **74**, 045808 (2006).
- [56] C. Wellenhofer, J. W. Holt, and N. Kaiser, *Phys. Rev. C* **93**, 055802 (2016).
- [57] C. Drisler, K. Hebeler, and A. Schwenk, *Phys. Rev. Lett.* **122**, 042501 (2019).
- [58] J. W. Holt, N. Kaiser, G. A. Miller, and W. Weise, *Phys. Rev. C* **88**, 024614 (2013).
- [59] J. W. Holt, N. Kaiser, and G. A. Miller, *Phys. Rev. C* **93**, 064603 (2016).
- [60] P. Bedaque and A. W. Steiner, *Phys. Rev. Lett.* **114**, 031103 (2015).
- [61] M. B. Tsang, J. R. Stone, F. Camera, P. Danielewicz, S. Gandolfi, K. Hebeler, C. J. Horowitz, J. Lee, W. G. Lynch, Z. Kohley *et al.*, *Phys. Rev. C* **86**, 015803 (2012).
- [62] S. M. Couch, *Astrophys. J.* **765**, 29 (2013).
- [63] L. F. Roberts, S. Reddy, and G. Shen, *Phys. Rev. C* **86**, 065803 (2012).
- [64] Y. Sekiguchi, K. Kiuchi, K. Kyutoku, and M. Shibata, *Phys. Rev. D* **91**, 064059 (2015).
- [65] A. S. Schneider, L. F. Roberts, and C. D. Ott, *Phys. Rev. C* **96**, 065802 (2017).
- [66] B. P. Abbott, R. Abbott, T. D. Abbott, F. Acernese, K. Ackley, C. Adams, T. Adams, P. Addesso, R. X. Adhikari, V. B. Adya *et al.* (LIGO Scientific Collaboration and Virgo Collaboration), *Phys. Rev. Lett.* **119**, 161101 (2017).